

Electromagnetic Signatures of Supermassive Binary Black Holes. I. Thermal Synchrotron, Self-Lensing Flares, and Jet Precession

HONG-XUAN JIANG ¹, XINYU LI ², YOSUKE MIZUNO ^{1, 3, 4, 5}, ZIRI YOUNSI,⁶ AND CHRISTIAN M. FROMM^{7, 5, 8}

¹*Tsung-Dao Lee Institute, Shanghai Jiao Tong University, Shengrong Road 520, Shanghai, 201210, China*

²*Department of Astronomy, Tsinghua University, 30 Shuangqing Rd, Beijing, 100084, China*

³*School of Physics and Astronomy, Shanghai Jiao Tong University, 800 Dongchuan Road, Shanghai, 200240, China*

⁴*Key Laboratory for Particle Physics, Astrophysics and Cosmology, Shanghai Key Laboratory for Particle Physics and Cosmology, Shanghai Jiao-Tong University, 800 Dongchuan Road, Shanghai, 200240, China*

⁵*Institut für Theoretische Physik, Goethe-Universität Frankfurt, Max-von-Laue-Straße 1, D-60438 Frankfurt am Main, Germany*

⁶*Mullard Space Science Laboratory, University College London, Holmbury St. Mary, Dorking, Surrey, RH5 6NT, UK*

⁷*Institut für Theoretische Physik und Astrophysik, Universität Würzburg, Emil-Fischer-Str. 31, D-97074 Würzburg, Germany*

⁸*Max-Planck-Institut für Radioastronomie, Auf dem Hügel 69, D-53121 Bonn, Germany*

ABSTRACT

The recent evidence for a nanohertz gravitational wave background from Pulsar Timing Arrays highlights the urgent need to identify electromagnetic counterparts to supermassive binary black holes. Here, we perform global 3D general relativistic magnetohydrodynamic (GRMHD) simulations of a secondary black hole (mass ratio $q = 0.1$) interacting with a Magnetically Arrested Disk around a primary black hole using a time-dependent superposed Kerr-Schild metric and post-processed general relativistic radiation transfer calculations based on thermal electron distribution function (eDF). We explore three orbital configurations: a vertical impact orbit, a coplanar embedded orbit, and a high-spin, eccentric, inclined scenario. Despite clear orbital periodicity and recurrent shock formation, the thermal synchrotron light curves frequently lack expected shock-induced flares. In vertical impacts, shock brightenings are typically sub-dominant to the stochastic MAD variability of the primary black hole, unless viewed at specific alignment phases. Conversely, coplanar orbits produce distinctive, rapid flares driven by gravitational self-lensing. We identify a frequency-dependent emission hierarchy: the primary black hole dominates sub-millimeter flux, while the secondary dominates near-infrared emission due to higher electron temperatures in thermal eDF. Finally, spin-orbit coupling drives Lense-Thirring precession, yielding twisted, wobbling jets reminiscent of OJ 287. Crucially, we demonstrate that intrinsic MAD turbulence may easily mask shock-induced flares at radio frequencies. We strongly advocate coordinated sub-millimeter and near-infrared monitoring to robustly isolate supermassive binary black hole self-lensing signatures.

1. INTRODUCTION

Supermassive binary black holes (SMBBHs) are a natural outcome of hierarchical galaxy growth and frequent mergers (M. C. Begelman et al. 1980; M. Volonteri 2010). Pulsar timing arrays (PTAs) are expected to be

most sensitive to the nanohertz stochastic gravitational-wave background from the cosmological SMBBH population (S. Burke-Spolaor et al. 2019; L. Z. Kelley 2025), and recent PTA data sets report compelling evidence for such a signal (G. Agazie et al. 2023, 2026; EPTA Collaboration et al. 2023a,b,c). Electromagnetic identification of SMBBHs is therefore increasingly important, both to interpret PTA detections and to enable multimessenger science with future space-based missions such as LISA (P. Amaro-Seoane et al. 2017; J. I. Thorpe et al. 2019).

In the electromagnetic domain, recurring (quasi-)periodic outbursts and jet modulations remain widely used diagnostics for SMBBH candidates, with the blazar OJ 287 as a canonical example (A. Sillanpaa et al. 1988,

Corresponding author: Hong-Xuan Jiang
hongxuan_jiang@sjtu.edu.cn

Corresponding author: Xinyu Li
xinyuli@tsinghua.edu.cn

Corresponding author: Yosuke Mizuno
mizuno@sjtu.edu.cn

1996; H. J. Lehto & M. J. Valtonen 1996; M. J. Valtonen et al. 2008, 2016; L. Dey et al. 2018; S. Laine et al. 2020). Recent polarimetric VLBI observations reveal a compact, twisted, magnetized inner jet and spatially resolved polarization variability in the innermost jet base (G.-Y. Zhao et al. 2022; J. L. Gómez et al. 2026). In addition, nearly edge-on SMBBHs can produce short-duration self-lensing flares when one BH magnifies emission from the other (e.g., D. J. D’Orazio & R. Di Stefano 2018; B. X. Hu et al. 2020); such events are expected to be sharply peaked and approximately time-symmetric, providing a clean signature against stochastic accretion variability (J. Davelaar & Z. Haiman 2022a,b; L. M. Krauth et al. 2024).

Physically interpreting these signatures requires strong-field general relativistic magnetohydrodynamic (GRMHD) modeling of accretion and jet launching near both BHs. Standard Newtonian circumbinary disk simulations capture large-scale gas dynamics but miss key relativistic effects near the horizons (e.g., P. C. Duffell et al. 2024; D. J. Muñoz et al. 2020). Full GRMHD simulations that evolve the plasma in a time-dependent binary spacetime are computationally expensive for long-duration, high-resolution studies (e.g., B. D. Farris et al. 2012; Z. B. Etienne et al. 2015; G. Fedrigo et al. 2024; V. Manikantan et al. 2025). A practical approach is to evolve GRMHD on an approximate, time-dependent BBH spacetime: post-Newtonian near-zone methods enabled early studies but required excising the cavity near the horizons (S. C. Noble et al. 2012; L. Combi et al. 2021), while a superposed Kerr–Schild construction enables long-duration, horizon-resolving simulations and shows good agreement with full numerical relativity (F. G. Lopez Armengol et al. 2021; L. Combi & S. M. Ressler 2024). Recent applications have begun to explore the impacts on magnetically arrested disks (MADs) and OJ 287-like disk crossings, finding signatures of enhanced accretion, outflows, and orbital precession (P. Suková et al. 2021; S. M. Ressler et al. 2024, 2025).

MADs, in which magnetic flux accumulates near the BH and powers efficient Blandford–Znajek jets (R. D. Blandford & R. L. Znajek 1977; A. Tchekhovskoy et al. 2011), can reproduce key observational features of M 87* including variability and polarization structure (R. Narayan et al. 2012; A. Sądowski et al. 2015; Event Horizon Telescope Collaboration et al. 2019a,b, 2021, 2025). However, the observable electromagnetic signatures of a secondary BH perturbing such an M 87*-like low-luminosity active galactic nuclei (LLAGN) system remain poorly quantified. We therefore use M 87* as a fiducial target to study a broader class of LLAGN host-

ing MAD-like, radiatively inefficient accretion flows, and to quantify how a secondary BH would perturb their multi-wavelength emission. In this Letter, we address this by performing controlled global 3D GRMHD simulations of a MAD torus perturbed by a companion with mass ratio $q = 0.1$ on a time-dependent approximate BBH metric, and connect the dynamics to observables via general relativistic radiative transfer (GRRT) post-processing across radio to near-infrared wavelengths. By moving beyond parameterized analytical models, these first-principles calculations reveal how intrinsic turbulent noise masks binary interaction signatures, establishing a rigorous predictive baseline for targeting SMBBHs with next-generation facilities like ngEHT and GRAVITY+.

2. NUMERICAL METHOD

We perform global 3D GRMHD simulations of a MAD torus perturbed by a secondary BH on a time-dependent binary spacetime. We adopt geometric units with $G = c = M_1 = 1$, where M_1 is the primary BH mass. The secondary mass is fixed to $M_2 = qM_1 = 0.1$, and we define $r_g \equiv GM_1/c^2$ as the gravitational radius of the primary. Table 1 summarizes the run suite; all binary runs adopt $q = 0.1$ and separation $d = 30 r_g$.

Following S. M. Ressler et al. (2024), we fix the primary BH at the coordinate origin and allow its spin axis, along with the corresponding jet and disk orientations, to precess due to spin-orbit coupling. We consider three binary configurations (runs VT, CP, and EP) and a single-BH baseline case (run BASE). Hereafter we refer to these configurations as runs VT, CP, EP, and BASE (Table 1). Runs VT and CP use a non-spinning primary ($a_1 = 0$) as controlled experiments: run VT is a vertical impact orbit ($i = 90^\circ$) and run CP is a coplanar embedded orbit ($i = 0^\circ$). Run EP adopts high spins ($a_1 = a_2 = 0.9375$) and an eccentric ($e = 0.3$), initially 90° tilted companion orbit, producing a strongly time-dependent, precessing configuration. To ensure a smooth dynamical transition, the simulation initially evolves a single primary BH. The secondary BH is then gradually introduced into the system, with its mass smoothly increasing from zero to $0.1 M$ during the interval $t = 10,000 M$ to $11,000 M$. Details of the GRMHD implementation are given in Appendix A.3.

To connect the dynamics to observables, we post-process GRMHD snapshots with general relativistic radiative transfer (GRRT) using BHOSS (Z. Younsi et al. 2012, 2020) in a fast-light approximation, adopting thermal synchrotron emission with a R - β prescription ($R_{\text{high}} = 10$ and $R_{\text{low}} = 1$) for electron thermodynamics (M. Mościbrodzka et al. 2016). Unless otherwise stated,

Table 1. Run suite. All binary runs adopt $q = 0.1$ and separation $d = 30 r_g$. Inclination is measured relative to the initial torus midplane. Run labels: **VT** = vertical impact, **CP** = coplanar embedded, **EP** = eccentric precessing (high-spin), and **BASE** = single-BH baseline.

run	a_1	a_2	Inclination (i)	Eccentricity (e)	Description
VT	0	0.9375	90°	0	Vertical impact (transient shock)
CP	0	0.9375	0°	0	Coplanar (persistently embedded)
EP	0.9375	0.9375	90°	0.3	High-spin, eccentric, precessing
BASE	0	—	—	—	Single BH

we use an edge-on viewing inclination $\theta_{\text{obs}} = 90^\circ$ and compare $\phi_{\text{obs}} = 0^\circ$ and 90° to isolate strong versus minimal line-of-sight alignment effects. Full GRRT equations and the detailed post-processing setup normalized to M 87* are summarized in Appendix A.4.

3. RESULTS

3.1. MHD process during BH-disk interaction

In runs **VT** and **CP**, we consider a Schwarzschild BH as primary, under which the secondary BH remains on an approximately circular and fixed orbit. In Fig. 1, we plot the accretion rate and magnetic flux through the event horizons of both BHs measured at the event horizon. For each BH, we construct the measurement surface in its local Kerr-Schild coordinates, accounting for the Lorentz boost due to orbital motion. The mass accretion rate is computed as

$$\dot{M} = - \int_S \rho u^r \sqrt{-g} d\theta d\phi, \quad (1)$$

where ρ is the rest-mass density, u^r is the radial component of the 4-velocity (with the gradient $\partial r / \partial x^i$ properly boosted to the lab frame), and $\sqrt{-g} d\theta d\phi$ is the invariant surface measure. The magnetic flux through the horizon is calculated by:

$$\Phi_B = \frac{1}{2} \int_S |b^r u^0 - b^0 u^r| \sqrt{-g} d\theta d\phi, \quad (2)$$

where b^μ is the 4-magnetic field in the fluid frame, related to the coordinate magnetic field B^i by $b^0 = u_i B^i$ and $b^i = (B^i + b^0 u^i) / u^0$, which corresponds to the magnitude of the dual Faraday tensor component $|*F^{rt}|$.

As shown in Fig. 1a, compared to the single-BH run **BASE**, run **VT** does not exhibit a clear long-term deviation in \dot{M} after the secondary BH is introduced. However, we can see a clear modulation of the primary BH accretion rate associated with the vertical passages of the secondary BH through the torus. In the zoomed-in panel (e), where we plot \dot{M} for both BHs, each time the secondary BH crosses the torus, the accretion rate of the primary BH shows a small bump followed by a decrease; the next passage produces a similar rise in \dot{M} , repeating this pattern in each impact. In contrast, run **CP** shows

an initially elevated \dot{M} following the introduction of the smaller BH, but this enhancement diminishes later and results in a slightly lower \dot{M} after $t = 15,000 M$. When secondary BH is first introduced, it interacts with the torus, which is similar to the torus-BH impacts in the run **VT**. It drives shocks which compress the gas and the funnel material toward the BH, temporarily increasing \dot{M} . However, over time, the secondary BH evacuates gas along its orbit, reducing the available supply for accretion. This depletion resembles the development of a low-density cavity commonly seen in circumbinary disk systems (e.g. D. J. Muñoz et al. 2020, 2019; P. C. Duffell et al. 2024). The difference is most pronounced in run **EP**. With a rapidly spinning primary BH, both the mass accretion rate and magnetic flux are lower than in the Schwarzschild cases (runs **VT**, **CP**, and **BASE**).

In Fig. 1c and d, we show the accretion rate and horizon-threading magnetic flux of the secondary BH. In run **VT** (black solid curves), both \dot{M} and Φ_B exhibit strongly periodic bursts that coincide with the secondary BH penetrating the torus. By contrast, run **CP** (red solid curves) displays a more irregular, stochastic evolution, consistent with MRI-driven turbulence. Although run **EP** is initialized with a 90° inclined companion orbit, the orbital plane undergoes substantial reorientation over time (Appendix B.4), alternating between more vertical and more coplanar phases. As a result, the accretion rate of the secondary BH \dot{M}_{BH2} enhancements are less sharply periodic than in run **VT**, yet remain more coherent than the fully stochastic behavior in run **CP**. The power spectrum of the secondary BH accretion rate is shown in Appendix B.1 (Fig. 6). Both run **VT** and run **CP** exhibit orbital-scale periodic variability, with different dominant harmonics reflecting the interaction geometry. Run **EP** shows mixed behavior consistent with its time-dependent orbital reorientation (Appendix B.4).

3.2. Observational signatures of runs **VT** and **CP**

To obtain the observational signature of the BH-disk interaction discussed in Sec. 3.1, we perform GRRT calculations on the GRMHD snapshots. Using the same BBH metric as the GRMHD simulation, we obtain the

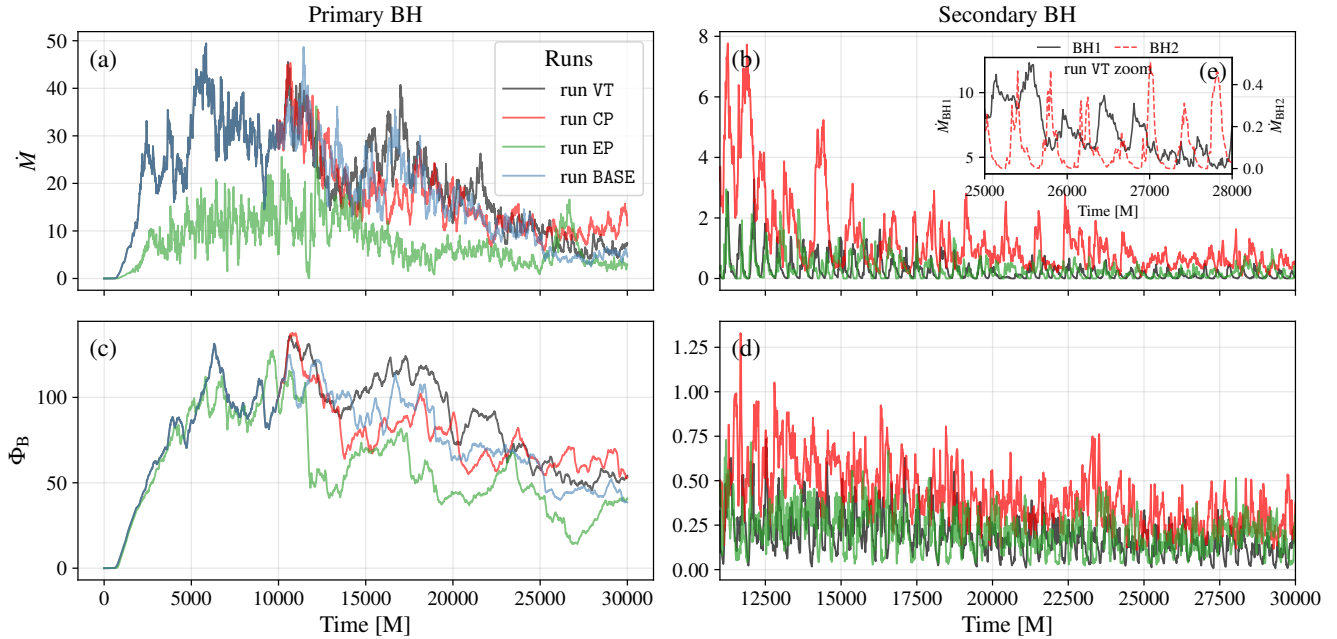


Figure 1. Mass accretion rates \dot{M} and magnetic fluxes Φ_B measured at the event horizons of the primary and secondary BHs. (a) Accretion rate of the primary BH, \dot{M}_{BH1} , for all runs (black: run VT; red: run CP; green: run EP; blue: run BASE). (b) Accretion rate of the secondary BH, \dot{M}_{BH2} , for runs VT, CP, and EP (colors as in panel a). (c) Horizon-threading magnetic flux of the primary BH, $\Phi_{\text{B,BH1}}$, for all runs. (d) Horizon-threading magnetic flux of the secondary BH, $\Phi_{\text{B,BH2}}$, for runs VT, CP, and EP. In all runs, the secondary BH is ramped in gradually over $t = 10,000$ – $11,000$ M; consequently, runs VT, CP, and BASE are identical for $t < 10,000$ M, and their divergences occur only after $t \gtrsim 11,000$ M. (e) Close-up view of the accretion rate evolution for run VT during $t \in [1.4, 1.6] \times 10^4$ M, comparing \dot{M}_{BH1} (black solid; left axis) and \dot{M}_{BH2} (red dashed; right axis).

thermal synchrotron light curves from runs VT, CP, and BASE in Fig. 2.

For the vertical-impact case (panels a and b in Fig. 2), to investigate the impact of gravitational lensing, two different azimuthal directions of line of sight (LOS) are considered: $\phi_{\text{obs}} = 90^\circ$ and $\phi_{\text{obs}} = 0^\circ$. For $\phi_{\text{obs}} = 90^\circ$ (blue solid line), the LOS is perpendicular to the orbital plane of the secondary BH, resulting in no lensing effects. In contrast, for $\phi_{\text{obs}} = 0^\circ$ (purple solid line), the observer and the binary BHs are aligned along the LOS twice per-orbit, leading to strong gravitational lensing effects during these alignments. Although the secondary BH exhibits highly periodic enhancements in its mass accretion rate (Fig. 1b), for $\phi_{\text{obs}} = 90^\circ$, where the lensing effect is absent, both the 230 GHz and 138 THz light curves remain stochastic and closely resemble the turbulence-driven variability of the single-BH case (run BASE). To quantitatively understand the effect of shock produced by the BH-disk interaction, we excise the plasma surrounding the secondary BH within a range of $r < 10 r_g$, effectively removing the major portion of the shock, as shown by the green solid lines in panels (a) and (b). At a specific time, for example, when $t = 27,840$ M, the shock induces a sharply spiked emission in the NIR light curve, which is ~ 3 times stronger

than the emission without the shock (see the zoomed-in panel in Fig. 2b). However, such pronounced effects are rare. Only a few shocks are strong enough to impact the 138 THz light curve noticeably. For most of the simulation time, the contribution from the shock is negligible, as evidenced by the light curves overlapping closely regardless of whether the shocked region is excised.

Luminous brightening happens when LOS is aligned with BBH position, the light curves develop extremely narrow, high-contrast flares, most prominently in the NIR band. This behavior is evident in panel b, where three sharp bursts appear on top of the underlying MAD-driven variability. The same phenomenology is also present in the coplanar run (panels (c) and (d)), in which both the 230 GHz and NIR light curves exhibit short, spiked flares. In this geometry, the spikes are naturally interpreted as self-lensing events occurring near the two alignment phases per orbit: the emission from the immediate vicinity of either BH is intermittently magnified when the observer and the two BHs approach near alignment along the LOS. In particular, the strongest amplification occurs when the primary BH lies between the secondary and the observer, since it acts as a much more efficient gravitational lens and can strongly magnify the secondary’s compact emission re-

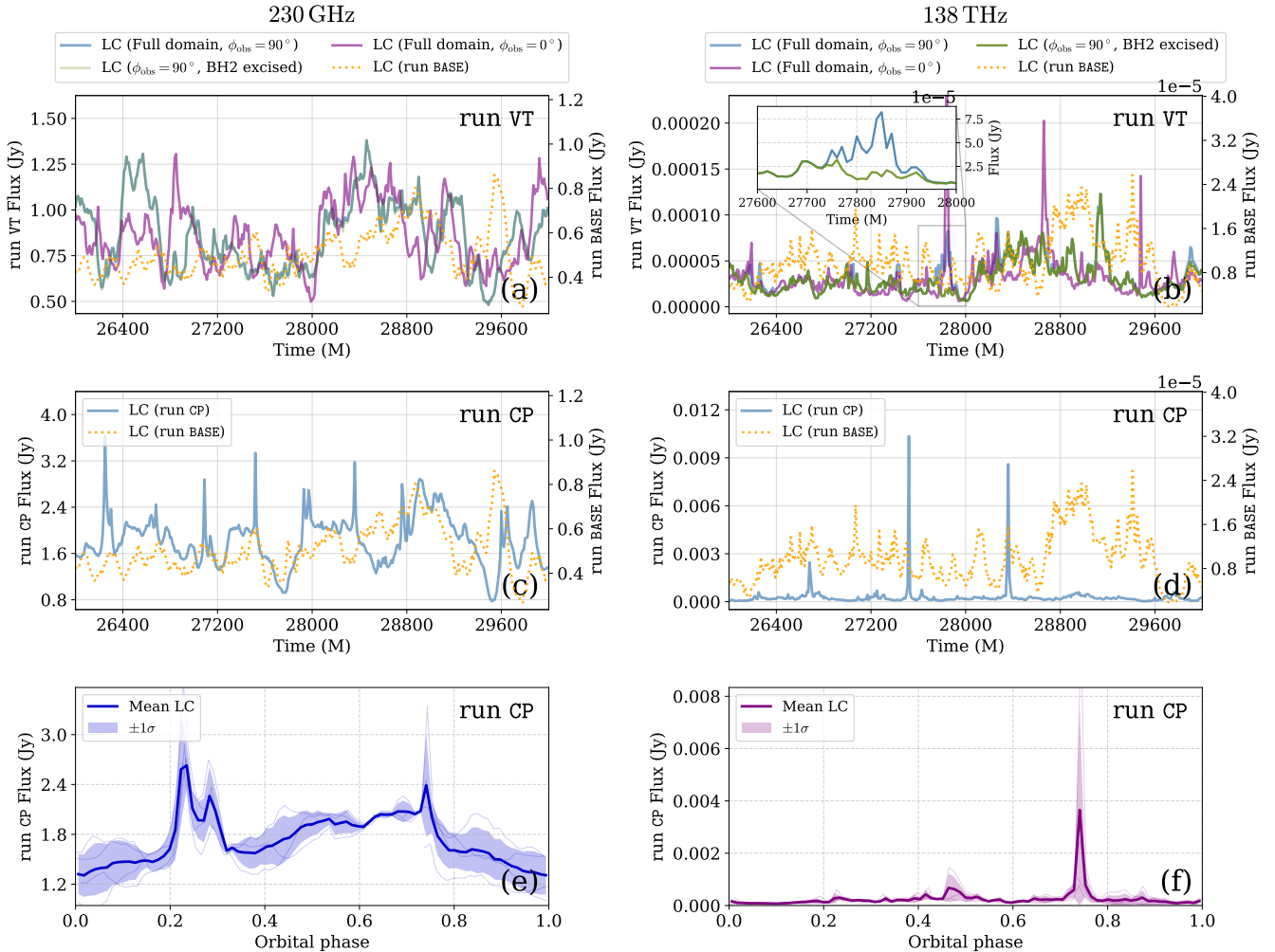


Figure 2. Thermal synchrotron light curves from GRRT post-processing. Panels (a)–(d) show $t = 26000$ – $30000 M$ time series, with the binary-run flux on the left axis and the single-BH control run **BASE** on the right axis (orange dotted). The top row shows run **VT**, and the middle row shows run **CP**. (a) run **VT** at 230 GHz for $\phi_{\text{obs}} = 90^\circ$ (blue) and $\phi_{\text{obs}} = 0^\circ$ (purple), and for $\phi_{\text{obs}} = 90^\circ$ with plasma within $r < 10 r_g$ of the secondary excised (green, lower opacity). (b) Same as (a) at 138 THz; the inset ($t = 27600$ – $28000 M$) highlights a particularly strong shock-driven flare during which the full-domain flux is $\sim 3\times$ higher than the excised case, whereas differences are otherwise modest. (c) run **CP** at 230 GHz compared to run **BASE**. (d) Same as (c) at 138 THz. (e,f) Orbit-folded run **CP** light curves versus orbital phase at 230 GHz and 138 THz. Faint curves show individual orbits; the thick curve and shaded band give the mean and $\pm 1\sigma$.

gion. These brief lensing episodes produce narrow bursts superposed on the stochastic, turbulence-driven baseline.

3.3. Synthetic horizon scale images of the BBH system

In Fig. 3, selected synthetic images of the BH shadow at different phase angles are presented. Panels (a)–(c) illustrate the process as the secondary BH approaches and enters the torus. Due to the large mass ratio ($q = 0.1$) of the two BHs, the secondary BH shadow is much smaller than the primary one but still visible as a bright spot. As it approaches and enters the torus, the interaction leads to the formation of a luminous bow shock, which then

evolves into a trailing tail. This luminous feature is a result of the plasma being compressed and heated by the intense gravitational forces from the secondary BH, and the shock wave propagating outward in the accretion flow (see more for plasma properties in Appendix B.3). Although the bow shock is clearly visible in GRMHD simulations, the contribution to total emission from the smaller BH is much weaker than that of the primary BH at sub-millimeter frequency (see in Fig. 2a and c).

In the middle row (panels (d)–(f)), we show the same set of snapshots but for a different LOS, with $\phi_{\text{obs}} = 0^\circ$. In this viewing angle, the observer becomes nearly aligned with the two BHs during the orbit, and

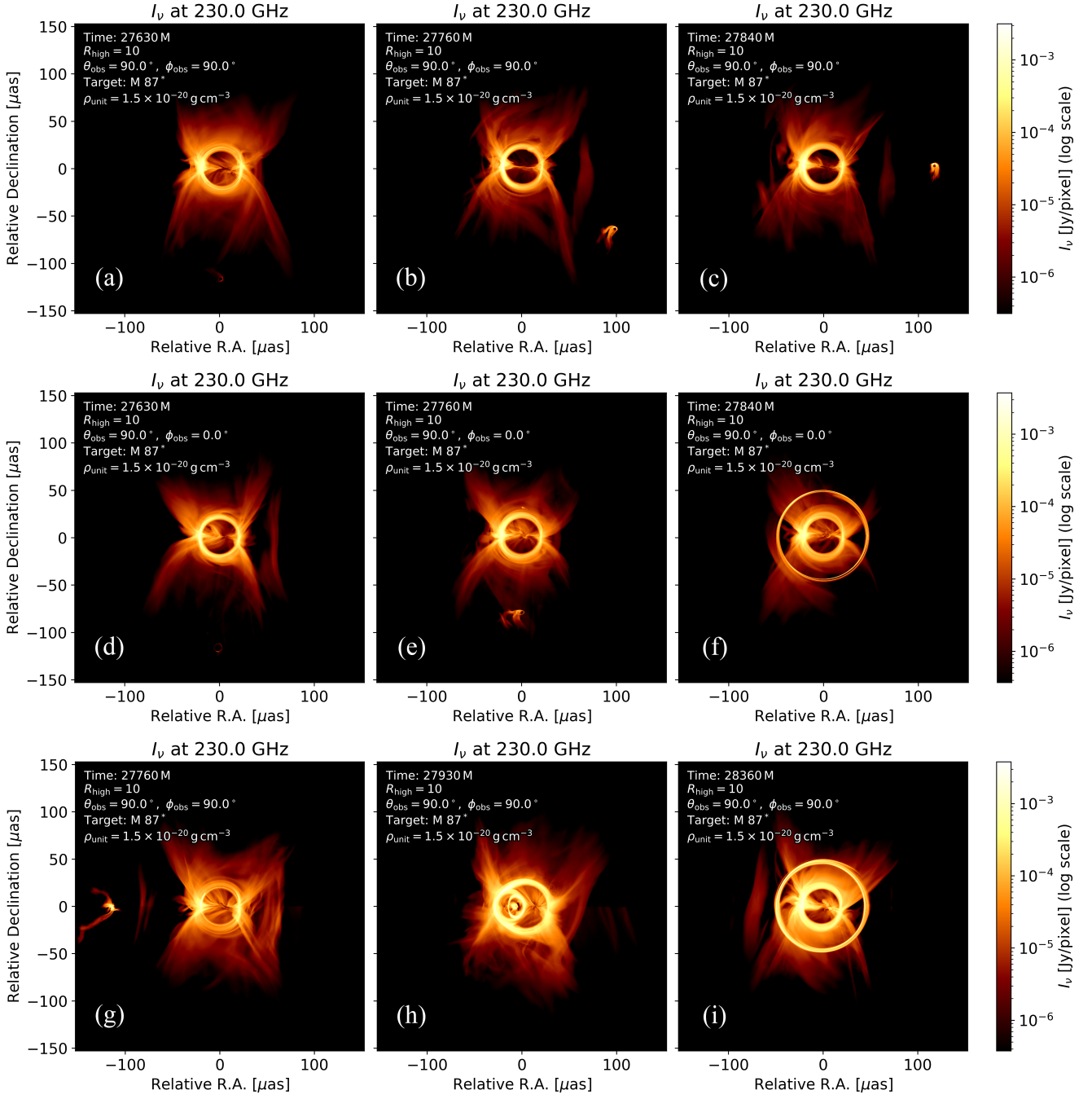


Figure 3. Synthetic horizon-scale total-intensity (I_ν) images at 230 GHz. Panels (a-c): run VT with $\phi_{\text{obs}} = 90^\circ$ at three representative times. Movie: <https://youtu.be/Z201nzWcnss>. Panels (d-f): run VT with $\phi_{\text{obs}} = 0^\circ$ at the corresponding epochs. Movie: https://youtu.be/R_2J4vxRqgg. Panels (g-i): run CP with $\phi_{\text{obs}} = 90^\circ$ at three representative times. Movie: <https://youtu.be/1NRrb8LMbWI>. The color scale shows I_ν in Jy pixel^{-1} (logarithmic), and each panel is labeled by its snapshot time and viewing geometry.

strong gravitational lensing can occur. In particular, at $t = 27,840 M$ the alignment is favorable for significant magnification of compact emission near the BHs, producing a pronounced transient brightening in the synthetic image. This lensing event corresponds directly to the luminous flare seen in the NIR light curve in Fig. 2c.

Finally, the lower middle row (panels (g)-(i)) of Fig. 3 presents synthetic images from the run CP. In this coplanar configuration, the secondary BH remains embedded within the torus and periodically passes from the foreground to the background relative to the primary along the LOS (panel (h) shows the secondary in front, while panel (i) shows it behind and correspondingly brighter). These passages create favorable alignment geometries that produce strong gravitational lensing, leading to pronounced, time-dependent distortions and magnification of the emission from the inner flow.

We create the corresponding orbit-folded light curves of run CP presented in Fig. 2e and f. It reveals a distinct difference between the sub-millimeter and NIR bands. At 230 GHz, the total flux is dominated by the accretion flow of the primary BH. However, when the secondary BH passes between the primary BH and the observer (orbital phase $\simeq 0.2-0.3$), the gravitational lensing effect becomes extreme. The secondary BH strongly magnifies the primary BH's photon ring emission, producing a pronounced brightening and a characteristic double-peaked profile (see Fig. 2e). This scenario corresponds to the shadow image in Fig. 3h, which displays a highly twisted photon ring and lensed image of the primary BH. In contrast, at 138 THz (Fig. 2f), the emission hierarchy is reversed. The secondary BH becomes the dominant source of radiation due to the significantly higher electron temperatures in its vicinity, while the emission coming from the accretion flows onto a primary BH fades. Consequently, the peak flux occurs when the secondary BH passes behind the primary BH (orbital phase ~ 0.72). In this configuration, the more massive primary BH lenses the compact emission of the secondary BH, focusing it into a prominent Einstein ring (as seen in Fig. 3i) and generating a sharp localized flare.

Notably, a mini-jet is launched from the secondary BH seen in Fig. 3g. As the secondary BH orbits, this outflow is sheared and twisted, and can feed back on the surrounding gas. Hydrodynamic studies show that sufficiently strong outflows can disrupt the gravitational wake and reduce, or even reverse, the effective drag force (“negative dynamical friction”) (X. Li et al. 2020), and that interacting outflows in binaries can yield a net positive torque that promotes orbital expansion (L. Wang & X. Li 2022). By analogy, an orbit-modulated outflow from the secondary BH may alter disk torques and

partially offset inward migration, which we leave to investigate in future work.

3.4. Morphology and Observational Signatures of the Precessing Binary

Similar to S. M. Ressler et al. (2024), spin-orbit coupling in our run EP drives a time-dependent reorientation of the primary BH spin axis, which in turn warps and twists the inner disk and jet orientation. To capture a more realistic and strongly time-dependent binary environment, run EP adopts a high-spin configuration for both BHs and an eccentric, highly inclined orbit.

Unlike runs VT and CP, the spinning primary BH in run EP induces strong frame dragging, and the associated Lense-Thirring (LT) torque drives pronounced precession of the secondary BH orbit. As the secondary BH circulates, spin-orbit coupling also causes the primary spin axis to vary in time (see the Appendix B.4 for a quantitative analysis of the disk and spin orientation evolution), leading to twisted and precessing jet structure. Fig. 4 shows synthetic 86 GHz images at three representative times, showing a changing jet orientation. The jet is bent and twisted, with a visibly wobbling nozzle that produces a time-dependent asymmetric emission pattern. Such precessing jet morphologies offer a natural explanation for the twisted jet structure seen in VLBI observations of blazars such as OJ 287 (G.-Y. Zhao et al. 2022; J. L. Gómez et al. 2026).

4. SUMMARY AND DISCUSSIONS

In this work, we perform global 3D GRMHD simulations coupled with GRRT calculations to investigate the dynamics of accretion flows and the observable signatures of SMBBHs embedded in MAD flows. Using an approximate time-dependent binary spacetime, we capture horizon-scale physics for a moderate mass-ratio system ($q = 0.1$). Our main findings are as follows.

1. *Dynamics-observable decoupling:* Even the secondary BH produces strong, periodic shock activity and accretion-rate bursts in the vertical-impact run VT, the thermal synchrotron emission often does not always exhibit corresponding bright flares. Instead, the light curves are usually dominated by stochastic MAD variability, with clear periodic features emerging mainly during favorable self-lensing alignments or in rare episodes of exceptionally strong shock heating.
2. *Geometry-dependent signatures:* Coplanar binaries (run CP) produce frequent, sharp self-lensing flares. At 230 GHz, the primary-flow emission dominates and can be lensed by the secondary,

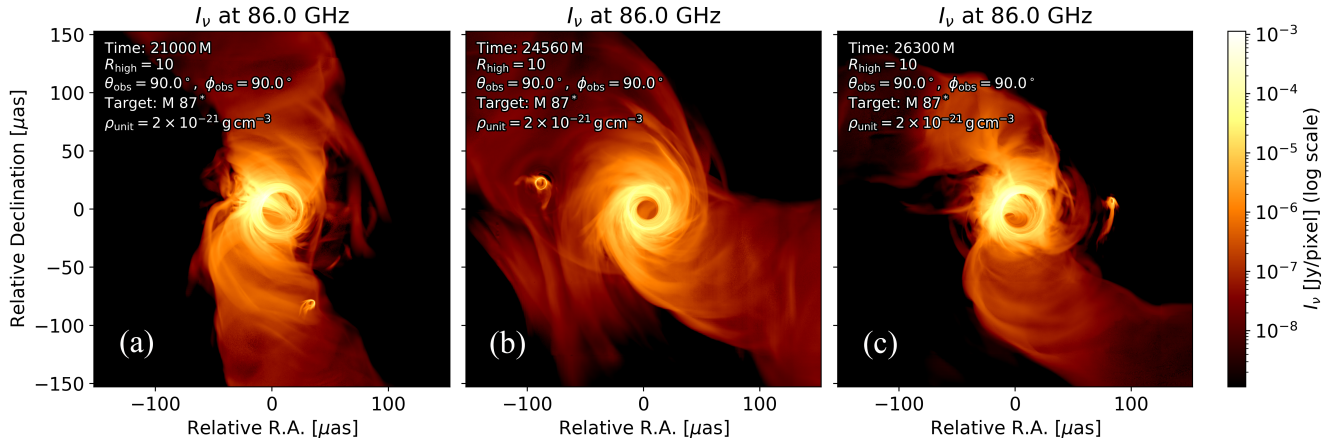


Figure 4. Synthetic total-intensity (I_ν) images from run EP at 86 GHz at three representative times. Panel (a) $t = 21,000 \text{ M}$; Panel (b) $t = 24,560 \text{ M}$; Panel (c) $t = 26,300 \text{ M}$. The color scale shows I_ν in Jy pixel^{-1} (logarithmic), and each panel is annotated with the snapshot time and viewing geometry. Movie: <https://youtu.be/dOQ8ppdLvWU>.

whereas in the NIR, the hotter, compact emission near the secondary can dominate and be lensed by the primary into brief, high-contrast bursts. Inclined, impacting orbits (run VT) generate bow shocks, but they yield observable flares primarily when the geometry is favorable.

3. *Jet precession:* In high-spin, eccentric run EP, torques from the secondary BH drive time-dependent reorientation of the primary BH spin, producing a wobbling twisted jet morphology that resembles VLBI observations such as OJ 287.

Overall, our results indicate that identifying SMBBHs will likely require combining time-domain diagnostics (e.g., short self-lensing spikes) with horizon-scale imaging of the inner accretion flow and jet. Next-generation VLBI facilities such as the EHT/ngEHT, together with coordinated multi-wavelength monitoring, will be key for separating binary signatures from intrinsic variability in a single AGN, while the ngVLA will provide complementary sensitivity to larger-scale jet structure and possible signatures of jet precession.

However, for distant candidates of SMBBH, direct resolution of the two components may remain challenging. Using OJ 287 as an illustrative case and adopting impact-binary scalings (L. Dey et al. 2019), the characteristic separation of the periastron is $\sim 9\text{--}15 R_S$ ($d \sim 0.016 \text{ pc}$). At $z \simeq 0.306$ (angular scale $\simeq 4.556 \text{ kpc arcsec}^{-1}$), this implies $\theta_{\text{sep}} \sim 3\text{--}6 \mu\text{as}$, below the $\sim 10\text{--}20 \mu\text{as}$ resolution of the current and near-term ground-based mm-VLBI. In this under-resolved regime, time-domain diagnostics may be more powerful: binary self-lensing can generate narrow, approximately symmetric flares near conjunction, but becomes prominent mainly for nearly edge-on viewing. Since

OJ 287 is a blazar with jet-dominated emission, its orientation and intrinsic jet variability may further dilute lensing contrast, making recurrent outbursts combined with jet-geometry changes attractive complementary probes. Extending baselines beyond Earth via future space-VLBI concepts (e.g., BHEX) could ultimately connect timing-based evidence to direct spatial constraints.

We note several limitations. Our GRRT modeling includes only thermal synchrotron emission and neglects inverse Compton scattering, which may contribute to shock-powered high-energy emission. We also focus on geometrically thick, radiatively inefficient flows; thin-disk systems such as OJ 287 (M. J. Valtonen et al. 2019) may exhibit different shock and variability properties. Finally, we emphasize edge-on configurations to maximize lensing; a broader inclination survey is needed to quantify detectability across the broader SMBBH population. This work only focuses on thermal eDF for the GRRT calculation, which is good enough for sub-millimeter emission, however, shock accelerates nonthermal emission leading to significant nonthermal emission at NIR band which will be investigated in our paper II.

ACKNOWLEDGMENTS

This research was supported by the National Key Research and Development Program of China (grant No. 2023YFE0101200), the National Natural Science Foundation of China (grant No. 12273022 and 12511540053), and the Shanghai Municipality Orientation Program of Basic Research for International Scientists (grant No. 22JC1410600). CMF is supported by the DFG research grant “Jet physics on horizon scales and beyond” (Grant No. 443220636) within the DFG research unit “Rela-

tivistic Jets in Active Galaxies" (FOR 5195). The simulations were performed on the TDLI-Astro, Pi2.0, and Siyuan-I cluster at Shanghai Jiao Tong University. The authors gratefully acknowledge Mr. Shuoqi Wang for his kind assistance with the GPU facilities.

Facilities:

Software:

AUTHOR CONTRIBUTIONS

APPENDIX

A. SIMULATION SETUP AND DETAILED PRESCRIPTIONS

A.1. Binary orbit and spin evolution

The dynamics of the binary black hole (BBH) system are governed by equations of motion derived from the post-Newtonian (PN) framework, incorporating both conservative and radiation-reaction terms as described in L. Blanchet (2014); M. Levi & J. Steinhoff (2015), with:

$$\dot{\mathbf{r}} = \mathbf{v}, \quad \dot{\mathbf{S}}_A = \boldsymbol{\Omega}_A \times \mathbf{S}_A, \quad A \in \{1, 2\}. \quad (\text{A1})$$

where \mathbf{r} is the position vector, \mathbf{v} is the velocity, and \mathbf{S}_A denotes the spin vector of the A -th black hole. We define the following kinematic variables required for the equations of motion:

$$r = |\mathbf{r}|, \quad \mathbf{n} = \frac{\mathbf{r}}{r}, \quad v^2 = \mathbf{v} \cdot \mathbf{v}, \quad \dot{r} = \mathbf{n} \cdot \mathbf{v}. \quad (\text{A2})$$

The acceleration is decomposed into four terms representing the non-spinning (ns) and spin-dependent contributions, further split into conservative (cons) and radiation-reaction (RR) effects:

$$\mathbf{a} = \mathbf{a}_{\text{ns}}^{\text{cons}} + \mathbf{a}_{\text{ns}}^{\text{RR}} + \mathbf{a}_{\text{spin}}^{\text{cons}} + \mathbf{a}_{\text{spin}}^{\text{RR}}. \quad (\text{A3})$$

These terms are expressed via Post-Newtonian (PN) expansions:

$$\mathbf{a}_{\text{ns}}^{\text{cons}} = \mathbf{a}_{0\text{PN}} + \mathbf{a}_{1\text{PN}} + \mathbf{a}_{2\text{PN}}, \quad (\text{A4})$$

$$\mathbf{a}_{\text{ns}}^{\text{RR}} = \mathbf{a}_{2.5\text{PN}}^{\text{RR}} + \mathbf{a}_{3.5\text{PN}}^{\text{RR}} + \mathbf{a}_{4\text{PN}}^{\text{RR}}, \quad (\text{A5})$$

$$\mathbf{a}_{\text{spin}}^{\text{cons}} = \mathbf{a}_{\text{SO}}^{1.5\text{PN}} + \mathbf{a}_{\text{SO}}^{2.5\text{PN}} + \mathbf{a}_{\text{SS}}^{2\text{PN}} + \mathbf{a}_{\text{SS}}^{3\text{PN}}, \quad (\text{A6})$$

$$\mathbf{a}_{\text{spin}}^{\text{RR}} = \mathbf{a}_{\text{SO}}^{2.5\text{PN,RR}} + \mathbf{a}_{\text{SO}}^{3.5\text{PN,RR}}. \quad (\text{A7})$$

Here, $\mathbf{a}_{\text{spin}}^{\text{cons}}$ and $\mathbf{a}_{\text{spin}}^{\text{RR}}$ account for spin-orbit (SO) and spin-spin (SS) interactions. The spin vectors precess with a frequency $\boldsymbol{\Omega}_A$ given by:

$$\boldsymbol{\Omega}_A = \boldsymbol{\Omega}_{A,\text{SO}}^{\text{NLO}} + \boldsymbol{\Omega}_{A,\text{SS}}^{\text{LO}} + \boldsymbol{\Omega}_{A,\text{SS}}^{\text{NLO}} + \boldsymbol{\Omega}_{A,\text{QM}}, \quad (\text{A8})$$

which encompasses geodetic and LT precession ($\boldsymbol{\Omega}_{A,\text{SO}}$), spin-spin interactions ($\boldsymbol{\Omega}_{A,\text{SS}}$), and quadrupole-monopole self-spin coupling ($\boldsymbol{\Omega}_{A,\text{QM}}$). In this context, LO (Leading Order) refers to the dominant contribution to the interaction, while NLO (Next-to-Leading Order) represents higher-order relativistic corrections that refine the system's overall description.

The initial tangential velocity v_ϕ for quasi-circular orbits is determined by solving the radial force balance equation using only the conservative terms:

$$a_r^{\text{cons}} + \frac{v_\phi^2}{r} = 0. \quad (\text{A9})$$

The full PN system is then integrated forward in time to evolve the binary orbit and spins.

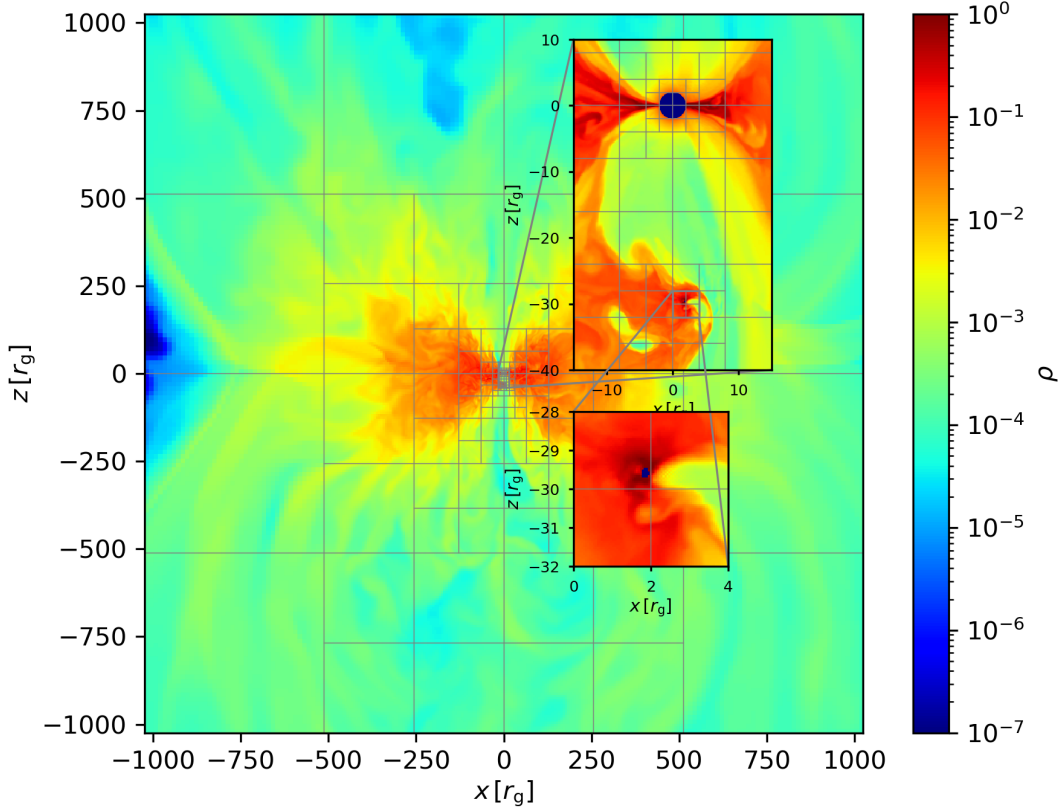


Figure 5. Gas density slice from run VT at $t = 26,410 M$ (edge-on slice), overlaid with the meshblock boundaries.

A.2. Superposed Kerr-Schild binary metric

We adopt the superposed Kerr-Schild construction (F. G. Lopez Armengol et al. 2021; L. Combi & S. M. Ressler 2024), in which the covariant metric is expressed as a Minkowski background plus Kerr-Schild perturbations from two boosted Kerr BHs,

$$g_{\mu\nu} = \eta_{\mu\nu} + \sum_{A=1}^2 H_A l_{\mu}^{(A)} l_{\nu}^{(A)}, \quad (\text{A10})$$

where H_A is the Kerr-Schild scalar for BH A and $l_{\mu}^{(A)}$ is the corresponding ingoing null covector. Orbital motion is incorporated by boosting each BH's Kerr-Schild data from its instantaneous comoving frame to the simulation frame,

$$l_{\mu}^{(A)} = (\Lambda_A)_{\mu}^{\alpha} l_{\alpha}^{(A,\text{rest})}, \quad (\text{A11})$$

with Λ_A the Lorentz boost determined by the instantaneous BH velocity from the PN trajectory.

A.3. GRMHD setup on a time-dependent superposed Kerr-Schild spacetime

Following F. G. Lopez Armengol et al. (2021); S. M. Ressler et al. (2024), the background spacetime is modeled using the superposed Kerr-Schild metric, with the BBH trajectory and spin evolution supplied by high-order PN evolution (L. Blanchet 2014; M. Levi & J. Steinhoff 2015); see Appendices A.2 and A.1 for details. The GRMHD equations are solved with the DynGRMHD module in AthenaK (J. M. Stone et al. 2024), adopting an ideal-gas equation of state with $\Gamma = 5/3$.

To capture both the global MAD accretion flow and the horizon-scale dynamics around the secondary BH, we employ static mesh refinement (SMR) together with adaptive mesh refinement (AMR), using a BH-tracking criterion to maintain uniform resolution around each horizon. The simulation domain is covered by 7 levels of SMR, with 3

additional levels of AMR that resolve the horizons, reaching a smallest cell size of $\Delta x_{\min} \equiv 0.05 r_g$ in the highest-refinement region. An example density slice from run VT illustrating the refinement layout and the boundary of meshblocks is shown in Fig. 5. Inside $1 GM_{1,2}/c^2$ of each BH, we excise the plasma in a floor condition.

In GRMHD simulations, we set the magnetization ceiling $\sigma_{\text{ceiling}} = 100$. We initialize the flow with a Fishbone–Moncrief hydrostatic equilibrium torus (L. G. Fishbone & V. Moncrief 1976) with parameters of $r_{\min} = 20 r_g$ and $r_{\max} = 40 r_g$, where $r_g = GM/c^2$, M is the mass of the primary BH. The torus is embedded with a poloidal magnetic field to reach the MAD regime. The magnetic field is initialized as

$$A_\phi \propto (\rho - 0.01)(r/r_{\text{in}})^3 \sin^3 \theta \exp(-r/400) \sin(2\pi(r - r_{\text{in}})), \quad (\text{A12})$$

with the field strength set by the minimum plasma $\beta_{\min} = 100$, where β is the ratio of gas pressure (p_{gas}) to magnetic pressure (p_{mag}).

A.4. GRRT equations, electron thermodynamics, and post-processing setup

GRRT is performed with BHOSS (Z. Younsi et al. 2012, 2020) using a fast-light approximation. We solve the general relativistic radiation transfer equation along null geodesics,

$$\frac{d\mathbf{S}}{d\lambda} = \mathbf{j} - \mathbf{K}\mathbf{S}, \quad (\text{A13})$$

where $\mathbf{S} = (I, Q, U, V)^\top$, \mathbf{j} is the emissivity vector, and \mathbf{K} contains absorption and Faraday terms. Electron temperatures are set using the R - β prescription (M. Mościbrodzka et al. 2016),

$$\frac{T_i}{T_e} = R_{\text{high}} \frac{\beta^2}{1 + \beta^2} + R_{\text{low}} \frac{1}{1 + \beta^2}, \quad (\text{A14})$$

where β is the plasma beta and $(R_{\text{high}}, R_{\text{low}}) = (10, 1)$ in our fiducial models, motivated by comparisons to two-temperature GRMHD results (H.-X. Jiang et al. 2023, 2024).

We compute synthetic observables by post-processing GRMHD snapshots with BHOSS, modified to ray-trace on the superposed Kerr-Schild spacetime in Cartesian coordinates. The observables are computed for an edge-on viewing inclination $\theta_{\text{obs}} = 90^\circ$, and we consider two azimuthal viewing angles, $\phi_{\text{obs}} = 0^\circ$ and 90° , to isolate cases with strong and minimal effects from line-of-sight, respectively. For the GRRT calculations, we adopt M 87* as a fiducial target, with BH mass $M_{\text{BH}} = 6.5 \times 10^9 M_\odot$ and source distance $d_{\text{BH}} = 16.8 \text{ Mpc}$. We exclude highly magnetized regions by applying a cutoff at $\sigma > 5$. The electron distribution function is assumed to be a thermal Maxwell–Jüttner distribution, while the impact of non-thermal electrons is left to be investigated in our future work.

We set the density normalization of the GRRT calculations by matching the single-BH baseline (run BASE) to a total flux of $\simeq 0.5 \text{ Jy}$ at 230 GHz for M 87*. For runs VT, CP, and BASE, we adopt $\rho_{\text{unit}} = 1.5 \times 10^{-20} \text{ g cm}^{-3}$, calibrated using snapshots from the quasi-steady interval $t = 25,000\text{--}30,000 M$. For run EP, we use a lower normalization, $\rho_{\text{unit}} = 2 \times 10^{-21} \text{ g cm}^{-3}$, to obtain a comparable total 230 GHz flux. For imaging, we use a field of view of $40 r_g \times 40 r_g$ and a fixed camera resolution of 1000×1000 pixels for all BHOSS images, which is sufficient to resolve the photon ring of the secondary BH.

B. APPENDIX INFORMATION

B.1. Power spectrum of the secondary accretion rate

Fig. 6 shows the power spectrum of the secondary BH mass accretion rates for the three binary runs. Both run VT and run CP exhibit periodic variability, yet display distinct characteristic frequencies. In run VT, where the secondary BH impacts the torus twice per orbit, the power spectrum shows a prominent peak aligned precisely with $2 \times f_{\text{orb}}$. In contrast, run CP reveals a characteristic frequency slightly lower than the orbital frequency, f_{orb} . Theoretically, the orbital motion of a secondary BH embedded in a perfectly axisymmetric flow should not induce quasi-periodic oscillations. However, MAD flows inherently develop non-axisymmetric structures (e.g., rotating magnetic flux bundles). Since these structures co-rotate with the flow, the secondary BH must “catch up” to the rotating pattern during each orbit, i.e., $f_{\text{obs}} \approx f_{\text{orb}} - f_{\text{flow}}$. Consequently, the effective interaction frequency is shifted to a value slightly lower than f_{orb} . In run EP, the power spectrum shows two clear peaks near f_{orb} and $2f_{\text{orb}}$, reflecting the fact that the companion alternates between phases that resemble embedded, coplanar motion (favoring a once-per-orbit modulation) and phases

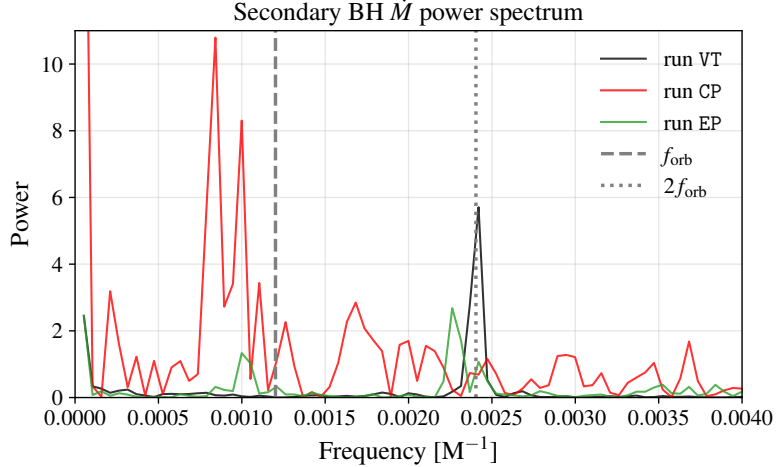


Figure 6. Power spectrum of mass accretion rate of the secondary BH $\dot{M}_{\text{BH}2}$. Solid curves show run VT (black), run CP (red), and run EP (green). Vertical gray dashed and dotted lines mark f_{orb} and $2f_{\text{orb}}$, respectively.

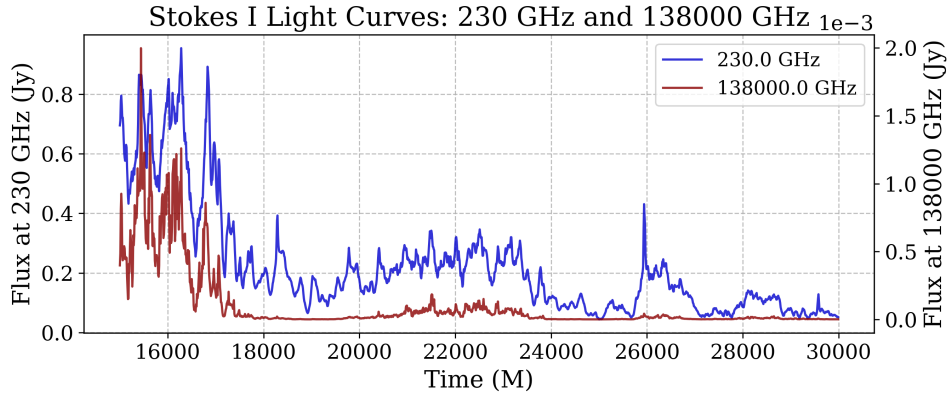


Figure 7. run EP Stokes-*I* light curves at 230 GHz (blue; left axis) and 1.38×10^5 GHz (brown; right axis).

with more vertical disk crossings (favoring a twice-per-orbit impact signature). This mixed behavior is consistent with the time-dependent reorientation of the orbit seen in Appendix B.4, which naturally imprints both harmonics rather than a single dominant frequency.

B.2. run EP light curves

Fig. 7 shows the light curves of the run EP at 230 GHz and 138 THz. Despite the pronounced jet and inner-flow reorientation, the thermal synchrotron emission does not show the regular quasi-periodic flaring seen in controlled runs VT and CP. Instead, the variability is largely stochastic. Only at $t \approx 26,000$ M the secondary passes behind the primary and becomes nearly aligned with the LOS, producing a bright self-lensing flare. At other epochs, shock activity can enhance emission, as in run VT, but these events are typically too weak to generate clearly separated spikes in the light curves. The run EP light curves at 230 GHz and 138 THz are shown in Appendix B.2 (Fig. 7), where we discuss their largely stochastic variability and the occasional strong self-lensing flare during near-alignment.

B.3. GRMHD slices and plasma dynamics

In Fig. 8, we show a time sequence of vertically sliced density maps for run VT (left column) and run CP (right column). For each snapshot, the slice is taken in the instantaneous plane spanned by the BH–BH separation vector and the global z -axis. We rotate the slicing plane every time so that its horizontal coordinate s always lies along the current line connecting the primary and secondary BHs. In this co-rotating slice, the primary BH remains fixed at

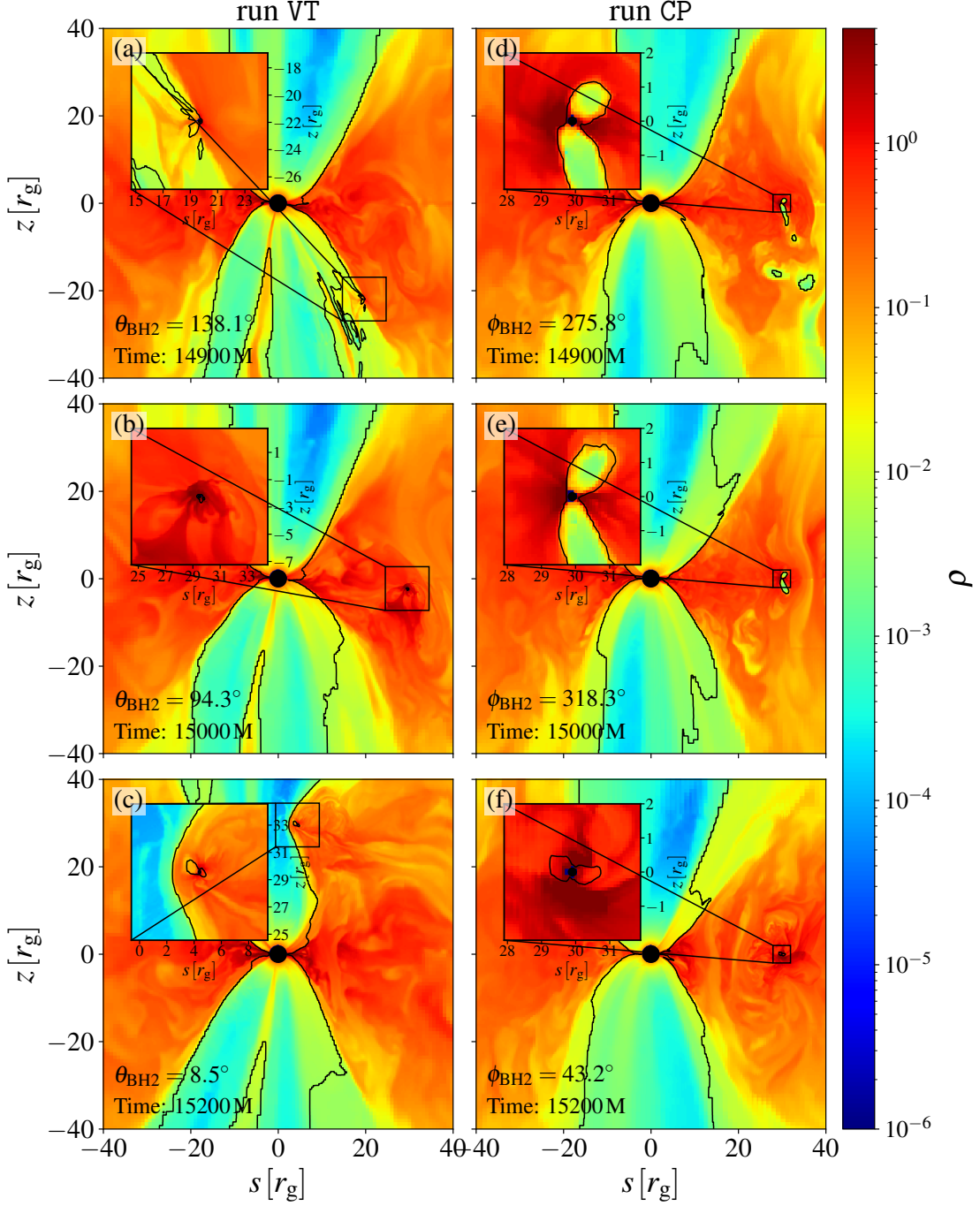


Figure 8. Evolution of the gas density (ρ) in run VT (left) and run CP (right) across three temporal snapshots: $t = 14,900$ M, $15,000$ M, and $15,200$ M. To capture the orbital dynamics, each panel displays a vertical (s, z) slice that dynamically tracks the secondary black hole. The horizontal coordinate s represents the radial distance along the instantaneous separation vector connecting the two masses, with the primary anchored at the origin ($s = 0$), while z denotes the vertical height in units of r_g . The logarithmic color map visualizes the density field, overlaid with solid black contours that delineate the $\sigma = 1$ magnetization boundary. Magnified inset panels highlight the immediate localized environment of the secondary. Each frame is annotated with the simulation time and the secondary's current orbital phase angle ($\theta_{\text{BH}2}$ for run VT; $\phi_{\text{BH}2}$ for run CP).

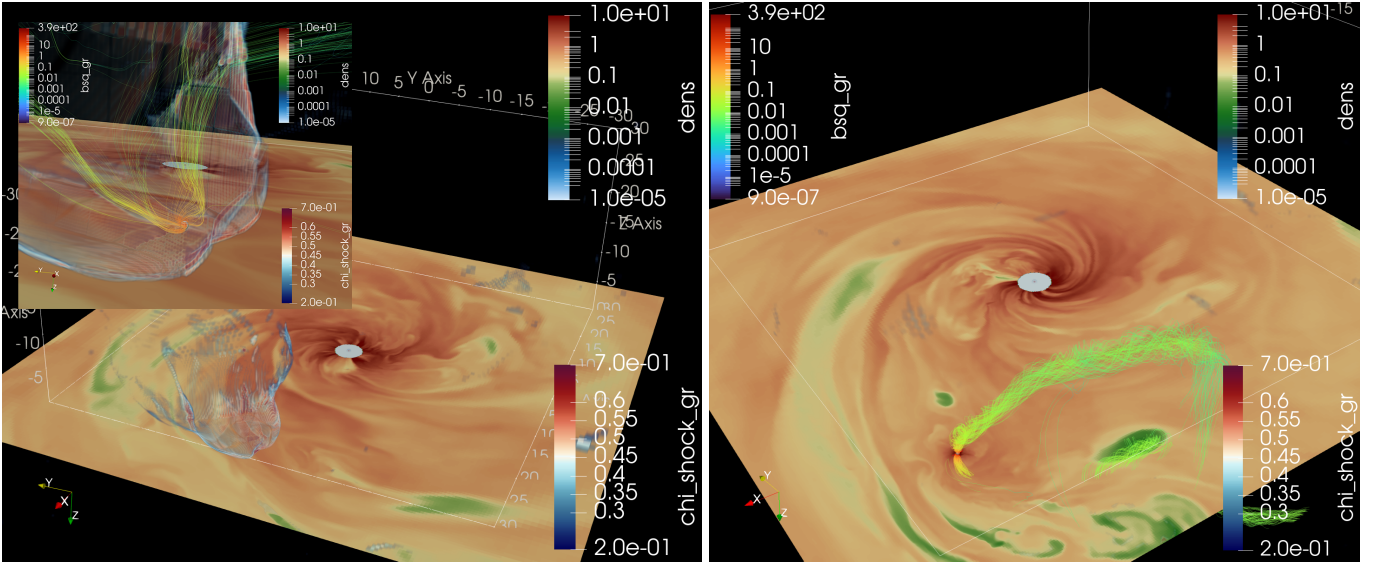


Figure 9. 3D visualization of the shock diagnostic and plasma structure near the secondary BH. Each panel shows a density slice together with volume rendering of the shock indicator χ_{shock} . Left: run VT snapshot; right: run CP snapshot. Insets and color bars indicate the plotted density and χ_{shock} ranges (and the displayed field-line overlay where shown).

$s = 0$, while the secondary appears at positive s at its instantaneous orbital phase (annotated in each panel by θ_{BH2} for run VT and ϕ_{BH2} for run CP). The colors show the density (ρ) on a logarithmic scale, and the black contour marks the magnetization $\sigma = 1$, which serves as a practical jet boundary (for either the primary jet or any outflow powered by the secondary). The run VT sequence captures a transient disk penetration: as the secondary plunges through and then emerges from the dense torus, it drives strong compressions, while simultaneously entraining a compact overdense cloud that remains bound briefly before being stripped and swept away once it enters the primary BH's jet. By contrast, in run CP the secondary stays embedded in the torus throughout this interval, maintaining a steady local gas supply. Consistent with this sustained feeding, density slices reveal episodic jet activity from the secondary BH: a collimated feature is visible at intermediate times (panels d–e), but it weakens and is absent by $t = 15,200 \text{ M}$ (panel f), indicating a quenched mini-jet state at that epoch.

Figure 9 provides a complementary three-dimensional view of the BH–disk interaction by visualizing the compressive structures and magnetic lines in the vicinity of the secondary BH. We introduce a dimensionless shock diagnostic,

$$\chi_{\text{shock}} \equiv \frac{\max(-\nabla_i v^i, 0)}{\ell_{\text{proper}}/c_{\text{fast}}}, \quad (\text{B15})$$

where $\nabla_i v^i$ is the covariant velocity divergence, ℓ_{proper} is the proper local cell length scale, and c_{fast} is the local fast magnetosonic speed. This quantity compares the compression time to the fast-mode crossing time: $\chi_{\text{shock}} \ll 1$ corresponds to weak compression, while $\chi_{\text{shock}} \gtrsim 1$ flags regions where compression is rapid enough to generate shock-like structures.

In the run VT snapshot (Fig. 9a), χ_{shock} shows a compact, high-compression region concentrated around the secondary, coincident with the strongest disturbance of the surrounding gas. The accompanying zoom-in, with magnetic field lines overlaid, shows pronounced bending and wrapping of the field in the compressed layer, consistent with flux-freezing as the secondary drives strong vertical interaction with the torus material. In the run CP snapshot (Fig. 9b), the same dynamic range produces little visible high volume χ_{shock} , indicating that the flow near the secondary is comparatively less compressive. In this case, the secondary largely co-moves with the local disk gas, reducing relative velocities and suppressing the formation of a strong shock. Despite the weaker shocks, the more persistent inflow onto the rapidly spinning secondary BH ($a = 0.9375$) supports intermittent mini-jet launching. As binary orbits, the resulting outflow is twisted and deflected by the ambient torus and the global field/jet environment (seen in the magnetic lines in Fig. 9b).

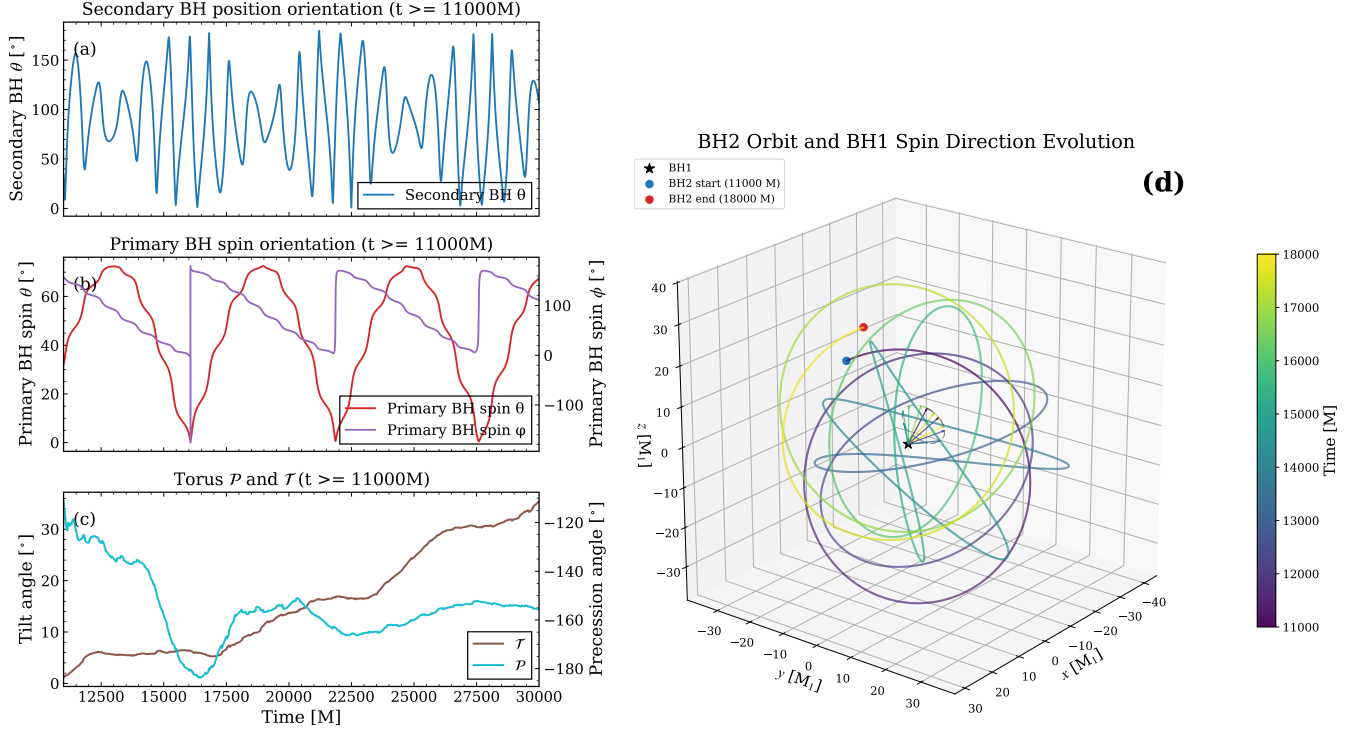


Figure 10. Orientation evolution in run EP for $t \geq 11,000 M$. (a) Polar angle θ of the secondary BH position vector. (b) Primary BH spin orientation: polar angle θ_{spin} (red; left axis) and azimuthal angle ϕ_{spin} (purple; right axis). (c) Torus angular-momentum orientation: tilt \mathcal{T} (brown; left axis) and precession angle \mathcal{P} (cyan; right axis), measured following P. C. Fragile & P. Aminos (2005); H.-X. Jiang et al. (2025). (d) 3D evolution of the secondary BH orbit together with the primary BH spin direction: the colored curve traces the secondary BH trajectory, the short vector anchored at the primary BH indicates the instantaneous primary BH spin direction.

B.4. Dynamical Evolution of BH Spin and Disk Orientation

To validate the physical origin of the precessing jet morphology observed in run EP, we quantify the time evolution of the position and orientations of the BHs and torus. Fig. 10 presents the position angles for the secondary BH orbit, the primary BH spin, and the torus angular momentum.

The first panel of Fig. 10 tracks the polar angle θ of the secondary BH’s position vector. The secondary BH is initialized on a highly inclined orbit with $i = 90^\circ$ relative to the initial torus midplane. As the system evolves ($t \geq 11,000 M$), θ develops large-amplitude oscillations, indicating strong nodal precession of the orbital plane driven by LT torques from the spinning primary BH. As a result, the orbit cyclically reorients, alternating between phases that are closer to vertical disk crossings and phases that are more nearly coplanar with the disk.

The second panel shows the evolution of the primary BH’s spin orientation, characterized by the polar angle θ_{spin} and azimuthal angle ϕ_{spin} . Although the primary BH is much more massive than the disk and the secondary BH, the cumulative torque from the orbiting companion induces a secular drift in the spin axis over long timescales. The spin axis precesses, with θ_{spin} and ϕ_{spin} showing coupled oscillations.

Panel c shows the time evolution of the torus angular-momentum orientation, characterized by the tilt angle \mathcal{T} and precession angle \mathcal{P} , measured using the same procedure as in H.-X. Jiang et al. (2025). The tilt of the torus increases secularly from a few degrees at $t \simeq 11,000 M$ to $\mathcal{T} \sim 30^\circ$ by $t \simeq 30,000 M$, indicating a gradual growth of the global misalignment relative to the $+z$ axis. Meanwhile, \mathcal{P} exhibits a pronounced early-time sweep followed by slower late-time evolution, suggesting that azimuthal reorientation becomes less rapid after the initial adjustment phase. In comparison of panels (b) and (c), the torus orientation tends to evolve in the same sense as the primary BH spin reorientation, consistent with the torus responding to the changing torque geometry imposed by the primary BH. However, the characteristic time scale of the primary BH spin precession is noticeably shorter: θ_{spin} and ϕ_{spin} vary rapidly and coherently, whereas \mathcal{T} and \mathcal{P} change more gradually, implying that the torus responds more slowly and cannot track the fastest components of the primary BH spin precession.

Panel (d) visualizes the coupled 3D evolution by overlaying the secondary BH orbital trajectory with the instantaneous primary BH spin direction. From $t \simeq 11,000\text{--}18,000 M$, the secondary BH follows a highly variable path, oscillating between the vertical and coplanar phases (consistent with Fig. 10a). During this interval, the primary BH spin precesses around a tilted axis, increasing the torus tilt angle seen in panel (c). This indicates that the torus angular momentum is gradually torqued to follow the evolving BH configuration, although its longer response time ensures that its precession lags behind the primary BH spin precession.

REFERENCES

- Agazie, G., Anumalapudi, A., Archibald, A. M., et al. 2023, *ApJL*, 951, L8, doi: [10.3847/2041-8213/acdac6](https://doi.org/10.3847/2041-8213/acdac6)
- Agazie, G., Anumalapudi, A., Archibald, A. M., et al. 2026, arXiv e-prints, arXiv:2601.09481, doi: [10.48550/arXiv.2601.09481](https://doi.org/10.48550/arXiv.2601.09481)
- Amaro-Seoane, P., Audley, H., Babak, S., et al. 2017, arXiv e-prints, arXiv:1702.00786, doi: [10.48550/arXiv.1702.00786](https://doi.org/10.48550/arXiv.1702.00786)
- Begelman, M. C., Blandford, R. D., & Rees, M. J. 1980, *Nature*, 287, 307, doi: [10.1038/287307a0](https://doi.org/10.1038/287307a0)
- Blanchet, L. 2014, *Living Reviews in Relativity*, 17, 2, doi: [10.12942/lrr-2014-2](https://doi.org/10.12942/lrr-2014-2)
- Blandford, R. D., & Znajek, R. L. 1977, *MNRAS*, 179, 433, doi: [10.1093/mnras/179.3.433](https://doi.org/10.1093/mnras/179.3.433)
- Burke-Spolaor, S., Taylor, S. R., Charisi, M., et al. 2019, *A&A Rv*, 27, 5, doi: [10.1007/s00159-019-0115-7](https://doi.org/10.1007/s00159-019-0115-7)
- Combi, L., Armengol, F. G. L., Campanelli, M., et al. 2021, *PhRvD*, 104, 044041, doi: [10.1103/PhysRevD.104.044041](https://doi.org/10.1103/PhysRevD.104.044041)
- Combi, L., & Ressler, S. M. 2024, arXiv e-prints, arXiv:2403.13308, doi: [10.48550/arXiv.2403.13308](https://doi.org/10.48550/arXiv.2403.13308)
- Davelaar, J., & Haiman, Z. 2022a, *PhRvD*, 105, 103010, doi: [10.1103/PhysRevD.105.103010](https://doi.org/10.1103/PhysRevD.105.103010)
- Davelaar, J., & Haiman, Z. 2022b, *PhRvL*, 128, 191101, doi: [10.1103/PhysRevLett.128.191101](https://doi.org/10.1103/PhysRevLett.128.191101)
- Dey, L., Valtonen, M. J., Gopakumar, A., et al. 2018, *ApJ*, 866, 11, doi: [10.3847/1538-4357/aadd95](https://doi.org/10.3847/1538-4357/aadd95)
- Dey, L., Gopakumar, A., Valtonen, M., et al. 2019, *Universe*, 5, 108, doi: [10.3390/universe5050108](https://doi.org/10.3390/universe5050108)
- D’Orazio, D. J., & Di Stefano, R. 2018, *MNRAS*, 474, 2975, doi: [10.1093/mnras/stx2936](https://doi.org/10.1093/mnras/stx2936)
- Duffell, P. C., Dittmann, A. J., D’Orazio, D. J., et al. 2024, *ApJ*, 970, 156, doi: [10.3847/1538-4357/ad5a7e](https://doi.org/10.3847/1538-4357/ad5a7e)
- EPTA Collaboration, Antoniadis, J., Babak, S., et al. 2023a, *A&A*, 678, A48, doi: [10.1051/0004-6361/202346841](https://doi.org/10.1051/0004-6361/202346841)
- EPTA Collaboration, InPTA Collaboration, Antoniadis, J., et al. 2023b, *A&A*, 678, A49, doi: [10.1051/0004-6361/202346842](https://doi.org/10.1051/0004-6361/202346842)
- EPTA Collaboration, InPTA Collaboration, Antoniadis, J., et al. 2023c, *A&A*, 678, A50, doi: [10.1051/0004-6361/202346844](https://doi.org/10.1051/0004-6361/202346844)
- Etienne, Z. B., Paschalidis, V., Haas, R., Mösta, P., & Shapiro, S. L. 2015, *Classical and Quantum Gravity*, 32, 175009, doi: [10.1088/0264-9381/32/17/175009](https://doi.org/10.1088/0264-9381/32/17/175009)
- Event Horizon Telescope Collaboration, Akiyama, K., Alberdi, A., et al. 2019a, *ApJL*, 875, L6, doi: [10.3847/2041-8213/ab1141](https://doi.org/10.3847/2041-8213/ab1141)
- Event Horizon Telescope Collaboration, Akiyama, K., Alberdi, A., et al. 2019b, *ApJL*, 875, L5, doi: [10.3847/2041-8213/ab0f43](https://doi.org/10.3847/2041-8213/ab0f43)
- Event Horizon Telescope Collaboration, Akiyama, K., Algaba, J. C., et al. 2021, *ApJL*, 910, L12, doi: [10.3847/2041-8213/abe71d](https://doi.org/10.3847/2041-8213/abe71d)
- Event Horizon Telescope Collaboration, Akiyama, K., Alentosa-Ruíz, E., et al. 2025, *A&A*, 704, A91, doi: [10.1051/0004-6361/202555855](https://doi.org/10.1051/0004-6361/202555855)
- Farris, B. D., Gold, R., Paschalidis, V., Etienne, Z. B., & Shapiro, S. L. 2012, *PhRvL*, 109, 221102, doi: [10.1103/PhysRevLett.109.221102](https://doi.org/10.1103/PhysRevLett.109.221102)
- Fedrigo, G., Cattorini, F., Giacomazzo, B., & Colpi, M. 2024, *PhRvD*, 109, 103024, doi: [10.1103/PhysRevD.109.103024](https://doi.org/10.1103/PhysRevD.109.103024)
- Fishbone, L. G., & Moncrief, V. 1976, *The Astrophysical Journal*, 207, 962, doi: [10.1086/154565](https://doi.org/10.1086/154565)
- Fragile, P. C., & Anninos, P. 2005, *ApJ*, 623, 347, doi: [10.1086/428433](https://doi.org/10.1086/428433)
- Gómez, J. L., Cho, I., Traianou, E., et al. 2026, *A&A*, 705, A23, doi: [10.1051/0004-6361/202555831](https://doi.org/10.1051/0004-6361/202555831)
- Hu, B. X., D’Orazio, D. J., Haiman, Z., et al. 2020, *MNRAS*, 495, 4061, doi: [10.1093/mnras/staa1312](https://doi.org/10.1093/mnras/staa1312)
- Jiang, H.-X., Mizuno, Y., Dihingia, I. K., et al. 2024, *A&A*, 688, A82, doi: [10.1051/0004-6361/202449681](https://doi.org/10.1051/0004-6361/202449681)
- Jiang, H.-X., Mizuno, Y., Fromm, C. M., & Nathanail, A. 2023, *MNRAS*, 522, 2307, doi: [10.1093/mnras/stad1106](https://doi.org/10.1093/mnras/stad1106)
- Jiang, H.-X., Mizuno, Y., Lai, D., Dihingia, I. K., & Fromm, C. M. 2025, *ApJ*, 995, 112, doi: [10.3847/1538-4357/ae19ee](https://doi.org/10.3847/1538-4357/ae19ee)
- Kelley, L. Z. 2025, arXiv e-prints, arXiv:2505.00797, doi: [10.48550/arXiv.2505.00797](https://doi.org/10.48550/arXiv.2505.00797)
- Krauth, L. M., Davelaar, J., Haiman, Z., et al. 2024, *PhRvD*, 109, 103014, doi: [10.1103/PhysRevD.109.103014](https://doi.org/10.1103/PhysRevD.109.103014)

- Laine, S., Dey, L., Valtonen, M., et al. 2020, *ApJL*, 894, L1, doi: [10.3847/2041-8213/ab79a4](https://doi.org/10.3847/2041-8213/ab79a4)
- Lehto, H. J., & Valtonen, M. J. 1996, *ApJ*, 460, 207, doi: [10.1086/176962](https://doi.org/10.1086/176962)
- Levi, M., & Steinhoff, J. 2015, *Journal of High Energy Physics*, 2015, 219, doi: [10.1007/JHEP09\(2015\)219](https://doi.org/10.1007/JHEP09(2015)219)
- Li, X., Chang, P., Levin, Y., Matzner, C. D., & Armitage, P. J. 2020, *MNRAS*, 494, 2327, doi: [10.1093/mnras/staa900](https://doi.org/10.1093/mnras/staa900)
- Lopez Armengol, F. G., Combi, L., Campanelli, M., et al. 2021, *ApJ*, 913, 16, doi: [10.3847/1538-4357/abf0af](https://doi.org/10.3847/1538-4357/abf0af)
- Manikantan, V., Paschalidis, V., & Bozzola, G. 2025, *PhRvD*, 112, 043004, doi: [10.1103/js22-3hfx](https://doi.org/10.1103/js22-3hfx)
- Mościbrodzka, M., Falcke, H., & Shiokawa, H. 2016, *A&A*, 586, A38, doi: [10.1051/0004-6361/201526630](https://doi.org/10.1051/0004-6361/201526630)
- Muñoz, D. J., Lai, D., Kratter, K., & Miranda, R. 2020, *ApJ*, 889, 114, doi: [10.3847/1538-4357/ab5d33](https://doi.org/10.3847/1538-4357/ab5d33)
- Muñoz, D. J., Miranda, R., & Lai, D. 2019, *ApJ*, 871, 84, doi: [10.3847/1538-4357/aaf867](https://doi.org/10.3847/1538-4357/aaf867)
- Narayan, R., Sądowski, A., Penna, R. F., & Kulkarni, A. K. 2012, *MNRAS*, 426, 3241, doi: [10.1111/j.1365-2966.2012.22002.x](https://doi.org/10.1111/j.1365-2966.2012.22002.x)
- Noble, S. C., Mundim, B. C., Nakano, H., et al. 2012, *ApJ*, 755, 51, doi: [10.1088/0004-637X/755/1/51](https://doi.org/10.1088/0004-637X/755/1/51)
- Ressler, S. M., Combi, L., Li, X., Ripperda, B., & Yang, H. 2024, *ApJ*, 967, 70, doi: [10.3847/1538-4357/ad3ae2](https://doi.org/10.3847/1538-4357/ad3ae2)
- Ressler, S. M., Combi, L., Ripperda, B., & Li, X. 2025, *ApJL*, 993, L22, doi: [10.3847/2041-8213/ae11ab](https://doi.org/10.3847/2041-8213/ae11ab)
- Sillanpaa, A., Haarala, S., Valtonen, M. J., Sundelius, B., & Byrd, G. G. 1988, *ApJ*, 325, 628, doi: [10.1086/166033](https://doi.org/10.1086/166033)
- Sillanpaa, A., Takalo, L. O., Pursimo, T., et al. 1996, *A&A*, 315, L13
- Sądowski, A., Narayan, R., Tchekhovskoy, A., et al. 2015, *MNRAS*, 447, 49, doi: [10.1093/mnras/stu2387](https://doi.org/10.1093/mnras/stu2387)
- Stone, J. M., Mullen, P. D., Fielding, D. B., et al. 2024, *arXiv e-prints*, arXiv:2409.16053, doi: [10.48550/arXiv.2409.16053](https://doi.org/10.48550/arXiv.2409.16053)
- Suková, P., Zajaček, M., Witzany, V., & Karas, V. 2021, *ApJ*, 917, 43, doi: [10.3847/1538-4357/ac05c6](https://doi.org/10.3847/1538-4357/ac05c6)
- Tchekhovskoy, A., Narayan, R., & McKinney, J. C. 2011, *MNRAS*, 418, L79, doi: [10.1111/j.1745-3933.2011.01147.x](https://doi.org/10.1111/j.1745-3933.2011.01147.x)
- Thorpe, J. I., Ziemer, J., Thorpe, I., et al. 2019, in *Bulletin of the American Astronomical Society*, Vol. 51, 77, doi: [10.48550/arXiv.1907.06482](https://doi.org/10.48550/arXiv.1907.06482)
- Valtonen, M. J., Lehto, H. J., Nilsson, K., et al. 2008, *Nature*, 452, 851, doi: [10.1038/nature06896](https://doi.org/10.1038/nature06896)
- Valtonen, M. J., Zola, S., Ciprini, S., et al. 2016, *ApJL*, 819, L37, doi: [10.3847/2041-8205/819/2/L37](https://doi.org/10.3847/2041-8205/819/2/L37)
- Valtonen, M. J., Zola, S., Pihajoki, P., et al. 2019, *ApJ*, 882, 88, doi: [10.3847/1538-4357/ab3573](https://doi.org/10.3847/1538-4357/ab3573)
- Volonteri, M. 2010, *A&A Rv*, 18, 279, doi: [10.1007/s00159-010-0029-x](https://doi.org/10.1007/s00159-010-0029-x)
- Wang, L., & Li, X. 2022, *ApJ*, 932, 108, doi: [10.3847/1538-4357/ac6ce6](https://doi.org/10.3847/1538-4357/ac6ce6)
- Younsi, Z., Porth, O., Mizuno, Y., Fromm, C. M., & Olivares, H. 2020, in *IAU Symposium*, Vol. 342, *Perseus in Sicily: From Black Hole to Cluster Outskirts*, ed. K. Asada, E. de Gouveia Dal Pino, M. Giroletti, H. Nagai, & R. Nemmen, 9–12, doi: [10.1017/S1743921318007263](https://doi.org/10.1017/S1743921318007263)
- Younsi, Z., Wu, K., & Fuerst, S. V. 2012, *A&A*, 545, A13, doi: [10.1051/0004-6361/201219599](https://doi.org/10.1051/0004-6361/201219599)
- Zhao, G.-Y., Gómez, J. L., Fuentes, A., et al. 2022, *ApJ*, 932, 72, doi: [10.3847/1538-4357/ac6b9c](https://doi.org/10.3847/1538-4357/ac6b9c)